

Tunneling rate constants for H₂CO + H on amorphous solid water surfaces

LEI SONG¹ AND JOHANNES KÄSTNER¹

¹*Institute for Theoretical Chemistry, University of Stuttgart,
Pfaffenwaldring 55, 70569 Stuttgart, Germany*

ABSTRACT

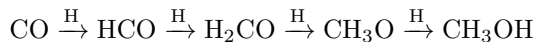
Formaldehyde (H₂CO) is one of the most abundant molecules observed in the icy mantle covering interstellar grains. Studying its evolution can contribute to our understanding of the formation of complex organic molecules in various interstellar environments. In this work, we investigated the hydrogenation reactions of H₂CO yielding CH₃O, CH₂OH and the hydrogen abstraction resulting in H₂ + HCO on an amorphous solid water (ASW) surface using a quantum mechanics/molecular mechanics (QM/MM) model. The binding energies of H₂CO on the ASW surface vary broadly from 1000 K to 9370 K. No correlation was found between binding energies and activation energies of hydrogenation reactions. Combining instanton theory with QM/MM modeling, we calculated rate constants for the Langmuir–Hinshelwood and the Eley–Rideal mechanisms for the three product channels of H + H₂CO surface reactions down to 59 K. We found that the channel producing CH₂OH can be ignored owing to its high activation barrier leading to significantly lower rates than the other two channels. The ASW surface influences the reactivity in favor of formation of CH₃O (branching ratio ~80%) and hinders the H₂CO dissociation into H₂+HCO. In addition, kinetic isotope effects are strong in all reaction channels and vary strongly between the channels. Finally, we provide fits of the rate constants to be used in astrochemical models.

Keywords: astrochemistry — molecular processes — ISM:molecules — tunneling rate constants — formaldehyde

1. INTRODUCTION

Formaldehyde (H₂CO) and complex organic molecules (COMs) are broadly observed in cold dense molecular clouds and high- or low-mass protostars. As a precursor to sugars formed through the formose reaction or as a precursor to amino acids they may have contributed to the origin of life on Earth (Maret, S. et al. 2004; Ford et al. 2004; Boogert et al. 2008; Herbst & van Dishoeck 2009; Velilla Prieto, L. et al. 2017). In dense molecular clouds, however, photolysis is insufficient, which might otherwise aid the formation of COMs. Therefore, it is interesting to study how such species can be formed without the presence of an embedded energy source. Formaldehyde is typically detected in the icy mantle covering interstellar grains and its formation is often attributed to the consecutive hydrogenation of carbon monoxide (CO) on the surface of amorphous solid

water (ASW) (Peters et al. 2013). The further hydrogenation of H₂CO on the ASW surface will yield the simplest alcohol, methanol (CH₃OH) which was repeatedly observed in dense clouds, both in the solid state and in the gas phase. The whole process can be described as (Tielens & Charnley 1997)



where only two steps, H + CO and H + H₂CO, have barriers. Solid methanol has been considered as a starting point for the formation of COMs. To explain the observed abundance of H₂CO and CH₃OH, several surface reactions need to be investigated and reliable reaction rates should be provided by experimental and/or theoretical studies.

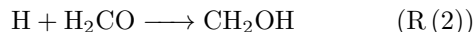
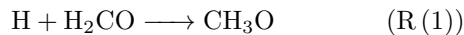
The formation of formaldehyde and methanol has been well-studied in experiments. Fedoseev et al. (2015) experimentally studied surface hydrogenation of CO molecules under dense molecular cloud conditions. It was shown that H₂CO and CH₃OH are formed along with molecules with more than one carbon atom. The latter probably form by recombination of HCO and

CH₃O. [Chuang et al. \(2016\)](#) performed laboratory experiments on H-atom addition and abstraction reactions in mixed CO, H₂CO and CH₃OH ices. They confirmed that H₂CO, once formed through CO hydrogenation, was subjected to H-atom addition reactions producing CH₃OH, but also yielded CO again via H-atom-induced abstraction reactions. At the same time, [Minissale et al. \(2016\)](#) gave their experimental results as H + H₂CO leading to two products, CO and CH₃OH. They found a strong competition between H-addition (CH₃OH formation), H-abstraction (CO formation), chemical desorption of H₂CO and other surface processes. However, experiments can only provide possible product channels and the relative amount of products. It is difficult to obtain the absolute values of rate constants.

A comprehensive theoretical study on the formation of H₂CO and CH₃OH was carried out by [Woon \(2002\)](#). He performed quantum chemical electronic structure calculations for reactions of H + CO and H + H₂CO in gas, with water clusters (H₂O)_n ($n \leq 3$) and on water ice. Without rate calculations, he qualitatively estimated the catalytic effect of surrounding water molecules by comparing the changes of activation energies. It was found that water molecules had little effect on the barrier of the H + CO reaction, but they modestly enhanced the addition reaction H + H₂CO \longrightarrow CH₃O and hindered the abstraction reaction H + H₂CO \longrightarrow H₂ + HCO. However, still no absolute rate constants were given. [Rimola et al. \(2014\)](#) studied the successive hydrogenation of CO on water ice to finally yield CH₃OH using quantum chemical simulations and astrochemical modeling. They compared the resulting abundances of CO, H₂CO, and CH₃OH with respect to water to those observed in low-mass protostars and dark cores. While they covered the hydrogenation reactions, they neglected hydrogen abstractions.

[Andersson et al. \(2011\)](#) calculated tunneling rate constants of H and D atom addition to CO at low temperatures. They provided the unimolecular and bimolecular rate constants for the H (D) + CO reaction at a temperature range of 5 to 180 K (20 to 180 K).

To fully cover the formation of CH₃OH in the interstellar environment, the other hydrogenation step with barrier, i.e. H + H₂CO, is required and tunneling rate constants should be provided at low temperature. In this work, we focus on three possible product channels of H + H₂CO as follows:



We study tunneling in those three reactions and provide rate constants for both, the Eley–Rideal mechanism and the Langmuir–Hinshelwood mechanism on an ASW surface. In addition, the corresponding deuterium-substituted reactions are studied and their rate constants are given as well. Finally, we provide fits of rate constants to be used in astrochemical models.

2. COMPUTATIONAL METHODS

We calculated the rates for the reactions R (1), R (2), and R (3) on an ASW surface model combining the quantum mechanics/molecular mechanics (QM/MM) method ([Warshel & Karplus 1972](#); [Warshel & Levitt 1976](#)) and instanton theory ([Langer 1967](#); [Miller 1975](#); [Coleman 1977](#); [Callan Jr. & Coleman 1977](#); [Althorpe 2011](#); [Richardson 2016](#)). The QM/MM method provides the potential energy, while the semi-classical instanton theory is used for rate calculations.

2.1. System Preparation

We prepared a thermalized ASW surface by classical molecular dynamics (MD) simulations with NAMD ([Phillips et al. 2005](#)). The initial sample was produced by VMD version 1.9.2 ([Humphrey et al. 1996](#)) with 9352 TIP3P ([Jorgensen et al. 1983](#)) water molecules in a slab of 85 Å \times 85 Å and a thickness of approximately 36 Å. We used periodic boundary conditions along all three Cartesian axes and kept a vacuum of around 70 Å thickness between the slabs. The system was treated in the canonical NVT ensemble. A Langevin dynamics simulation was performed firstly at 300 K for 100 ps followed by an instantaneous quenching to 10 K for 20 ps to produce a thermally equilibrated bulk amorphous solid water at low temperature. We cut a hemisphere with a radius of 34 Å to be used in the QM/MM model.

In order to locate different types of binding sites on the ASW surface, the H₂CO molecule was placed at 113 initial positions for minimization on a regular 2D-grid with step size of 2 Å covering the central circle area of the ASW hemisphere with a radius of 12 Å. For each of total 113 initial positions, the H₂CO molecule was placed 2.5 Å above the ASW surface. Each H₂CO molecule and its surrounding water molecules within 6 Å belonged to QM region (typically about 23 molecules), while the water molecules between 6 Å and 12 Å away from the H₂CO molecule were in the active MM region (typically about 160 molecules). The other water molecules, farther than 12 Å from H₂CO, were frozen.

2.2. QM/MM Method

The computational requirements for an accurate quantum mechanical (QM) method is prohibitive for geometry optimization and tunneling rate calculations on a system with more than 9000 atoms. Force field methods are cheap enough but generally inapplicable for chemical reactions. In this study, we use a state-of-the-art hybrid QM/MM simulation which combines the accuracy of the QM method and the speed of the force field (MM) approach. We treated the reactants H, H₂CO and their immediate environment with density functional theory (DFT) and described more distant water molecules by the TIP3P force field (Jorgensen et al. 1983). Van der Waals parameters for H and H₂CO were chosen in analogy to the CHARMM22 force field (MacKerell Jr. et al. 2004) in the QM/MM treatment.

The hybrid QM/MM simulations were carried out with the ChemShell (Sherwood et al. 2003; Metz et al. 2014) interface using additive QM/MM coupling. The interactions between QM and MM subsystems were handled in the electrostatic embedding scheme where MM atoms can polarize the electrons in the QM subsystem.

The level of theory for the QM region was chosen according to benchmark calculations performed in the gas phase. We first optimized the reactant, transition states and products of the three reactions R (1), R (2), and R (3) in the gas phase using the functional B3LYP-D3 (Becke 1993; Lee et al. 1988; Grimme et al. 2010) and the def2-TZVPD basis set (Rappoport & Furche 2010a). Then, the activation energies were calculated using explicitly correlated unrestricted coupled-cluster with singles and doubles excitations including perturbative treatment of triple excitations, (U)CCSD(T)-F12, (Adler et al. 2007; Knizia et al. 2009) based on a restricted Hartree-Fock (RHF) reference function and the cc-pVTZ-F12 basis (Peterson et al. 2008) as reference and with different DFT functionals. The PWB6K-D3/def2-TZVP (Zhao & Truhlar 2005; Grimme et al. 2010; Weigend & Ahlrichs 2005) level resulted in the most accurate activation energies for all three reactions in comparison with the (U)CCSD(T) reference as shown in Sec. 3.1, so this DFT level was applied in all following QM calculations. Energetic data are given in Kelvin, rounded to 10 K.

The quantum chemical program package NWChem 6.6 (Valiev et al. 2010) was used for the QM calculations while DL-POLY (Smith et al. 2002) built into ChemShell was used for the MM region. The open source DL-FIND (Kästner et al. 2009) optimizer was used for geometry optimization such as searching for binding sites, transition states using the dimer method (Henkelman & Jónsson 1999; Kästner & Sherwood 2008), and instanton pathways with a modified

Newton-Raphson approach (Rommel et al. 2011; Rommel & Kästner 2011). For the TS searches and the instanton calculations, the QM part was restricted to the adsorbate and one water molecule, for instanton searches the active part as well.

2.3. Instanton Theory

Tunneling rate constants in this work were calculated using instanton theory (Langer 1967; Miller 1975; Coleman 1977; Callan Jr. & Coleman 1977; Althorpe 2011; Richardson 2016) based on Feynman path integral theory in its semiclassical approximation. In general, it is only applicable below the crossover temperature T_c (Gillan 1987):

$$T_c = \frac{\hbar\omega_b}{2\pi k_B} \quad (1)$$

where \hbar is the reduced Planck constant, ω_b corresponds to the absolute value of the imaginary frequency at the transition structure, and k_B is the Boltzmann constant. The semiclassical nature of instanton theory offers a reasonable ratio of accuracy versus computational cost which is appropriate to the reactions with small organic molecules on the ASW surface. At a given temperature, the instanton itself is the tunneling path with the highest statistical weight. It can be located using transition state searching methods implemented in the DL-FIND optimizer. Integrating along this path and combining it with the partition function of reactant state, we can compute the instanton rate constants considering quantum effects such as zero point vibrational energy (ZPE) and atom tunneling (Rommel et al. 2011; Rommel & Kästner 2011). In this work, for reaction R (1) instantons were discretized to 78 images down to 83 K and 154 images below. For reaction R (2), 78 images were used down to 124 K and 154 images below. In reaction R (3) we used 78 images down to 111 K and 154 images below that. Branching ratios R were calculated by $R_i = k_i/(k_1 + k_2 + k_3)$ from the rate constants k_i .

3. RESULTS AND DISCUSSION

3.1. Benchmark Calculations

Benchmark calculations were performed to identify an accurate DFT level for binding site optimization, transition state search and instanton rate calculations. We applied the B3LYP-D3/def2-TZVPD level for the optimization of the reactant, transition states and products in the gas phase and used the resulting geometries to calculate the activation energies for three product channels on the (U)CCSD(T)-F12/cc-pVTZ-F12 level and with various DFT functionals with two different basis

sets, def2-TZVP (Weigend & Ahlrichs 2005) and def2-SVPD (Rappoport & Furche 2010b). The resulting activation energies are listed in Table 1. Compared with the (U)CCSD(T)-F12/cc-pVTZ-F12 result as the reference, the functional PWB6K-D3 (PWB6K functional with D3 dispersion correction) with the def2-TZVP basis set gave the closest activation energies for all three product channels with a relative deviation smaller than 7%. The results from other functionals had much larger deviations, some of which with opposite signs are qualitatively wrong, such as PBE96-D3, SSB-D-D3, TPSS-D3 and TPSSH-D3. We chose PWB6K-D3/def2-TZVP as the proper DFT level and re-optimized all species at this level. The activation energies at (U)CCSD(T)-F12/cc-pVTZ-F12 and PWB6K-D3/def2-TZVP levels were recalculated and listed at the last two lines in Table 1. The different geometries resulted in slightly different activation energies. However, PWB6K-D3/def2-TZVP still gave good results (within a maximum of 220 K deviation, 9% relative deviation) compared to the reference UCCSD(T)-F12/cc-pVTZ-F12 data.

3.2. H_2CO Binding Sites and Binding Energies

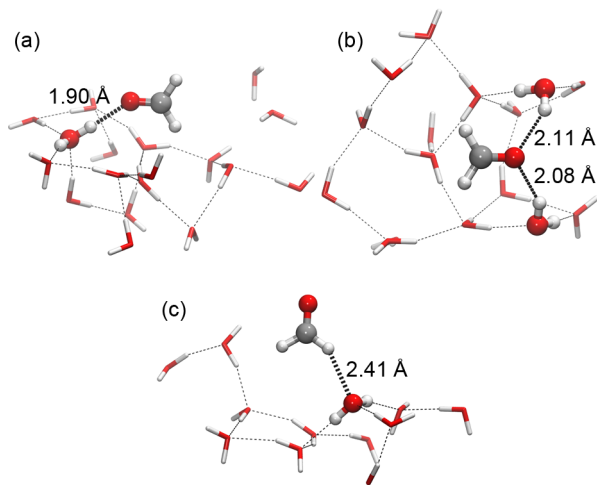


Figure 1. Three different H_2CO binding types on the amorphous solid water surface. Only QM molecules are shown. The H_2CO molecule and water molecules directly connected via hydrogen bonds are shown as balls and sticks. Bond lengths are given in Å.

All three reactions originate from H_2CO bound to the ASW surface. Thus, we first investigated possible binding sites and associated binding modes and energies. The H_2CO molecule was initially placed 2.5 Å above the ASW surface. Local minimum searches were started from 113 H_2CO initial positions. Out of these, 81 cases converged to physically meaningful local minima. They are categorized in three different types of binding modes,

visualized in Fig. 1. In this figure, we only show the molecules in the QM region, while the calculations were performed for the full QM/MM model. Type (a) is the major binding mode, 89% of the cases were found in that mode. The H_2CO accepts one hydrogen bond at its O atom. The bond lengths of the hydrogen bonds vary from 1.80 Å to 2.50 Å with an average of 1.97 Å. There were 7 cases (9%) belonging to type (b). In this case, the O end of the H_2CO molecule accepted two hydrogen bonds from two different water molecules. The remaining two cases (2%) belonged to type (c). Here, H_2CO donates a hydrogen bond to an O atom of water. These rather weak hydrogen bonds had lengths of 2.41 Å and 2.89 Å.

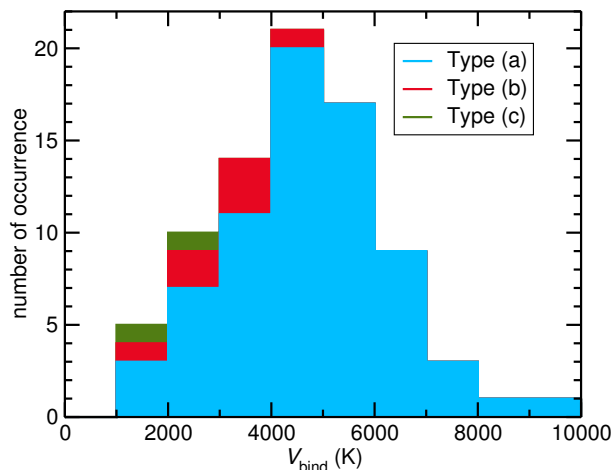


Figure 2. The distribution of H_2CO binding energies on the amorphous solid water surface at the PWB6K-D3/def2-TZVP/MM level of theory.

The binding energy V_{bind} of H_2CO is the potential energy required to disassemble the H_2CO molecule from the ASW surface to the gas phase including the relaxation of the surface. Figure 2 illustrates the binding energy distribution of H_2CO molecules on the ASW surface using the 81 successful cases. The distribution of binding energies corresponding to binding site type (a) is broad, ranging from 1000 to 9370 K with the largest fraction between 4000 and 5000 K. V_{bind} for all sites of type (a) is larger than 1200 K. There were only 9 cases of binding energies belonging to type (b) and type (c). They are rather weakly bound, with binding energies below 5000 K. These binding energies were obtained without consideration of the zero point vibrational energy (ZPE). We calculated the ZPE contributions for 5 cases. Taking ZPE into account reduces the binding energy by 580 to 920 K.

Table 2. Comparison of transition states for reactions R (1), R (2) and R (3) in gas and on the amorphous solid water surface. Energies (ER process) are given in K, bond distances d in Å, frequencies in cm⁻¹ and the temperature in K.

| site | reaction | V_{bind} | d | ω_b | V_{act} | E_{act} | T_c |
|-------|----------|-------------------|-------|------------|------------------|------------------|-------|
| gas | R (1) | | 1.855 | 840 | 1620 | 2160 | 192 |
| | R (2) | | 1.515 | 1521 | 4780 | 5210 | 348 |
| | R (3) | | 1.043 | 1599 | 3320 | 2470 | 366 |
| ASW 1 | R (1) | | 1.848 | 831 | 1420 | 1900 | 190 |
| | R (2) | 4600 | 1.488 | 1637 | 5220 | 5670 | 375 |
| | R (3) | | 1.022 | 1663 | 4030 | 3030 | 381 |
| ASW 2 | R (1) | | 1.853 | 793 | 1470 | 1920 | 182 |
| | R (2) | 5420 | 1.490 | 1626 | 5200 | 5620 | 372 |
| | R (3) | | 1.034 | 1567 | 3200 | 2270 | 359 |
| ASW 3 | R (1) | | 1.848 | 832 | 1410 | 1890 | 191 |
| | R (2) | 4270 | 1.515 | 1525 | 6480 | 6670 | 349 |
| | R (3) | | 1.044 | 1453 | 4590 | 3640 | 333 |
| ASW 4 | R (1) | | 1.854 | 819 | 1380 | 1870 | 188 |
| | R (2) | 5580 | 1.491 | 1619 | 5780 | 6090 | 371 |
| | R (3) | | 1.021 | 1665 | 4850 | 3680 | 381 |
| ASW 5 | R (1) | | 1.853 | 813 | 1100 | 1640 | 186 |
| | R (2) | 6080 | 1.507 | 1544 | 5190 | 5620 | 354 |
| | R (3) | | 1.034 | 1598 | 3920 | 2970 | 366 |

3.3. H₂CO + H Transition States

We investigated the H + H₂CO transition states for the three product channels both in gas phase and on the ASW surface. From the dominant binding type (a) as shown in the Fig. 1, we selected 5 binding sites with binding energies between 4200 and 6100 K to perform transition state optimizations using the QM/MM model. For each binding site, we found transition states TS1, TS2 and TS3 corresponding to reaction channels R (1), R (2), and R (3), respectively. The results are given in Table 2. The label ASW n ($n = 1 - 5$) is used to distinguish transition states based on different binding sites. The distance d measures the distance from the incoming H atom, specifically the C-H distance for R (1), the O-H distance for R (2), and the H-H distance for R (3). For comparison, the transition states of the gas phase reactions are provided in this table as well. The label V_{act} refers to the activation energy as potential energy difference, the label E_{act} indicates that the difference in vibrational zero point energy was taken into account as well.

From a classical perspective, H addition to C, R (1), has the lowest activation energies and is expected to be the dominant reaction channel while the H addition to

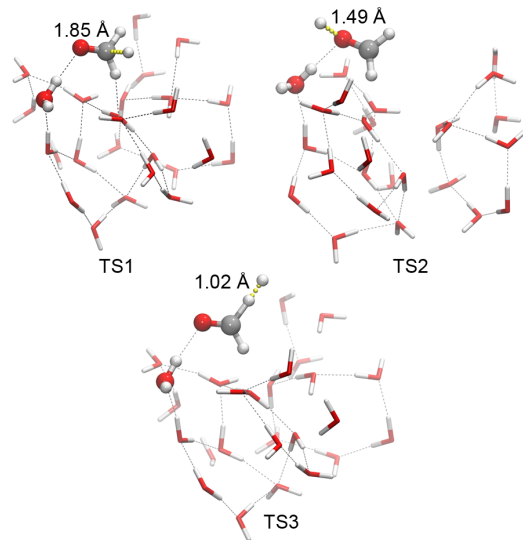


Figure 3. Optimized geometries of the transition states TS1, TS2 and TS3 for the reactions H + H₂CO on the amorphous solid water surface ASW 1 yielding CH₃O, CH₂OH and H₂ + HCO. In the TS search, the ball-and-stick molecules were in the QM region, while others are in the MM active region. Forming bonds are indicated by yellow dots.

O, R (2), has the highest activation energies and will happen in negligible amounts only. The H abstraction reaction, R (3), has a medium barrier height. Transition structures are shown in Fig. 3.

Compared with transition state geometries in the gas phase, the ones on the ASW surface always have shorter bond lengths along the reaction coordinates (H-C for TS1, H-O for TS2, and H-H for TS3, see Fig. 3), i.e. are later transition states. The exception is ASW 3 for TS2 and TS3, which are very slightly earlier transition states than the gas-phase ones. The effect of the ASW surface is to lower the barrier for R (1) and increase the barriers for R (2) and R (3). Thus, it promotes the formation of the more complex molecules CH₃O and CH₃OH and hinders the destruction of H₂CO to HCO. The reason is probably that the more protonated species CH₃O and CH₃OH are also more polar than HCO and therefore form more stable hydrogen bonds to the water environment.

All three reactions are exothermic, the most stable product is CH₂OH. Including ZPE, the reaction energy of R (1) is -12,510 K in the gas phase and -12,160 K on ASW in the binding site ASW 1. For R (2) the values are -14,980 K and -14,660 K. Reaction R (3) is much less endothermic with a gas-phase reaction energy of -7430 K and a surface reaction energy (with H₂ desorbed into the gas phase) of -6220 K. Thus, under ther-

modynamic control, the main product of hydrogenation of H_2CO would be CH_2OH .

3.4. Tunneling Rate Constants

Starting from transition states TS1, TS2 and TS3, we calculated tunneling rate constants for reactions R(1), R(2), and R(3) both in the gas phase and on the ASW surface using instanton theory. From Table 2 it is clear that the difference between the different adsorption sites is small. Therefore, we restricted the following analysis to site ASW 1. We provide surface instanton tunneling rate constants from just below the individual crossover temperatures down to 59 K, 75 K, and 59 K for the three product channels in supplementary machine-readable files. In the case of the gas-phase reaction, the lowest temperatures are 68 K, 62 K and 65 K. Below that, the tunneling energy dropped below the energy of the reactants and bimolecular rate constants are not accessible any more. For the surface reactions, we considered both the Eley–Rideal mechanism (ER) and the Langmuir–Hinshelwood mechanism (LH). The results are shown in Fig. 4, where they are also compared to UMIST and OSU parameterizations for R(3). We used hollow and solid markers to distinguish gas phase and surface reactions and labeled blue circles, red triangles and green diamonds for reactions R(1), R(2), and R(3) separately. The markers designate the gas phase and surface instanton rate constants while the lines correspond to the fits described in detail in Sec. 4.

Fig. 4 shows the rate constants and the results of the fits. The significant flattening of the Arrhenius curves indicates strong quantum tunneling effects in all three reactions. It is obvious that reaction R(2), forming CH_2OH , is the slowest reaction both in the gas phase and on the ASW surface owing to its high barriers of 5210 K and ~ 6000 K for those two situations. The rate constant of R(2) is about four orders of magnitude lower than those of R(1) and R(3) at low temperature.

The rate constants of R(1) and R(3) are similar in magnitude. In the gas phase, the hydrogen abstraction reaction R(3), forming $\text{H}_2 + \text{HCO}$ has larger rate constants than the hydrogen addition reaction R(1), forming CH_3O , at temperatures below 180 K. This is due to the stronger tunneling effects in R(3). The activation energy of R(3) is with 2470 K slightly higher than that of R(1) with 2160 K, see Table 2. Thus, at high temperature, when tunneling is suppressed, R(1) is faster. It should be noted here, that the hydrogen additions, R(1) and R(2) can, actually, only happen on the surface because of the limited efficiency of dissipation of the reaction energy in the gas phase.

On the ASW surface, the situation between R(1) and R(3) is reversed. The reaction R(1), forming CH_3O , is the preferred channel compared to hydrogen abstraction R(3) because of catalytic effects of the ASW surface. As shown in Table 2, the ASW surface decreased the bimolecular activation energy of R(1) from 2160 K to 1900 K (for binding site ASW 1, the values are similar for the other sites), while it raised the activation energy of reaction R(3) from 2470 K to 3030 K. That is to say, the ASW surface increased the difference in barrier heights between R(1) and R(3) from 310 K to 1130 K. To explain that, we calculated the intrinsic reaction coordinate (IRC) to show the barrier shapes for R(1) and R(3) both in gas and on the ASW. The IRC data are shown in Fig. 5. Note that these are potential energies and do not include ZPE. The ASW-barrier of R(1) is lower, but a little bit broader than the gas-phase one, while the ASW-barrier of R(3) is higher and narrower than that of the gas phase. It demonstrates that the ASW catalytic influence on the barrier height increases the rate of R(1) while its influence on the barrier width increases R(3). Including tunneling at the temperatures considered here, the effect on the height dominates, R(1) is the most effective reaction channel. The ASW surface promotes the formation of the radical CH_3O at the low temperatures of the interstellar medium, which is expected to increase the the yield of methanol and other more complex radicals and molecules. The reason, again, is probably that the polar water environment stabilizes the polar CH_3O (gas-phase dipole moment of 2.0 Debye) more efficiently than the comparatively less polar HCO (1.7 Debye).

It may be argued that the hydrogenation reactions of CO are more likely to happen on a CO ice surface than on ASW. In dense clouds, however, one can expect even a CO surface to already contain a significant part of impurities bearing OH groups, like methanol. Such an environment is expected to have a similar effect on the reactions studied here as ASW.

In panel (a) of Fig. 4, we show the bimolecular instanton rate constants. These data represent the ER mechanism, in which one reactant (H_2CO) is adsorbed on the surface and reacts with a second reactant (H atom) that approaches directly from the gas phase, related to a biomolecular reaction between the adsorbate-surface system and the incoming atom.

Unimolecular rate constants, which relate to the LH mechanism, are shown in panel (b) of Fig. 4. The LH mechanism is expected to dominate on the ASW surface at low temperature. In that case, an encounter complex of H with H_2CO on the ASW surface reacts to CH_3O , CH_2OH or $\text{H}_2 + \text{HCO}$ bound on the ASW surface in the

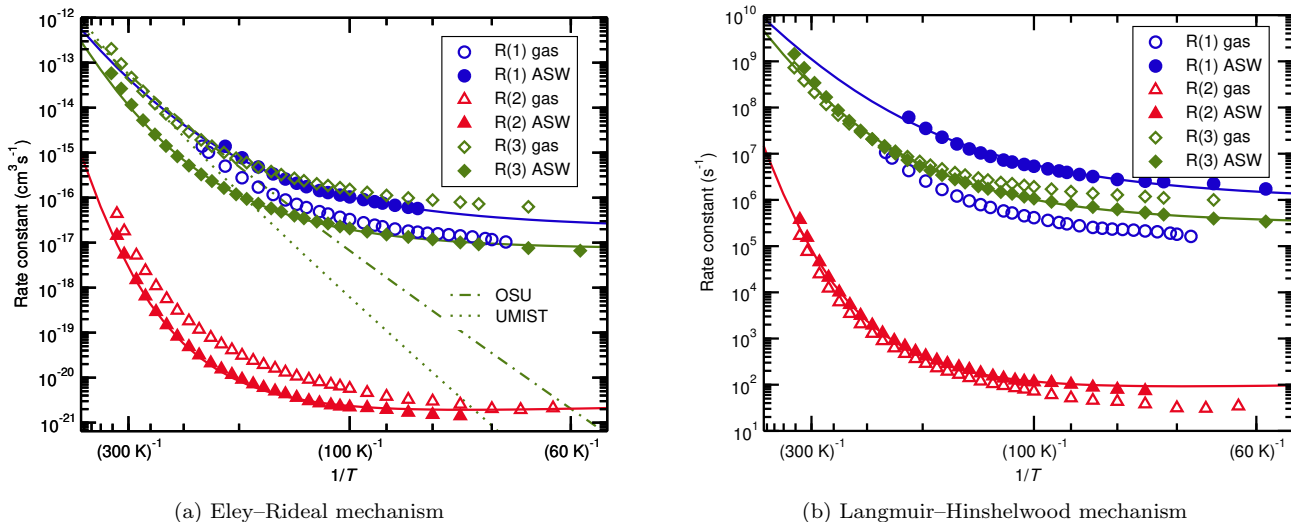


Figure 4. Instanton rate constants labeled as different markers and fitted lines for the reactions of $\text{H} + \text{H}_2\text{CO}$ yielding CH_3O (R (1)), CH_2OH (R (2)), and $\text{H}_2 + \text{HCO}$ (R (3)) in gas and on the amorphous solid water surface. OSU and UMIST gas-phase data for R (3) are shown for comparison.

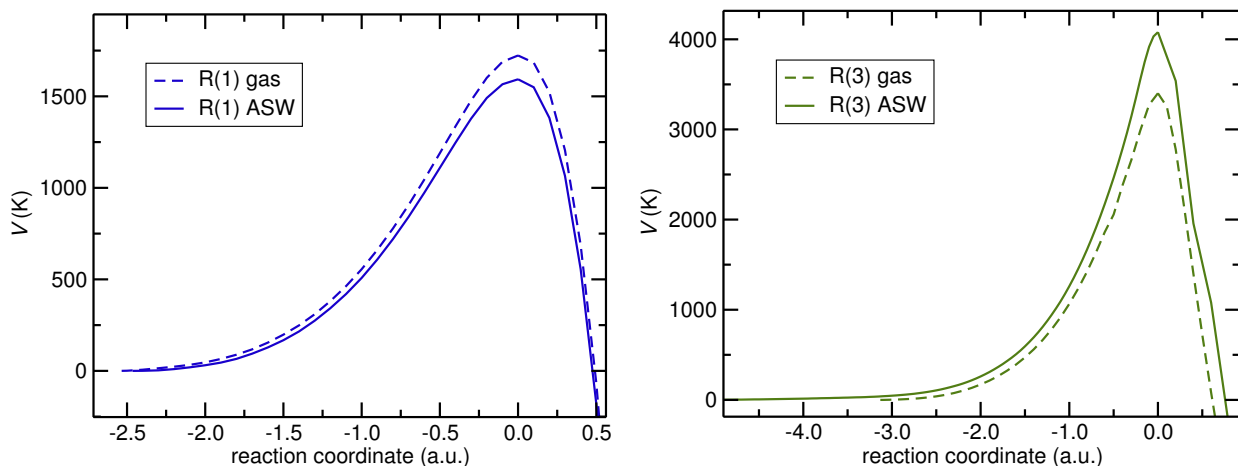


Figure 5. The minimum energy paths of the reactions of $\text{H} + \text{H}_2\text{CO} \longrightarrow \text{CH}_3\text{O}$ and $\text{H} + \text{H}_2\text{CO} \longrightarrow \text{H}_2 + \text{HCO}$ in the gas phase and on the amorphous solid water surface.

three product channels. The activation energies E_{act} are 1890 K, 5660 K, and 3030 K in those three reactions, respectively. The unimolecular rate constants behave similarly to the bimolecular ones. Again, ASW leads to a preference of R (1) over R (3) in contrast to the gas phase data. R (2) is also negligible for the unimolecular case.

In Fig. 6 we show the branching ratios for the three reactions for the LH mechanism on an ASW surface. At $T = 200$ K, R (1) accounts for about 85% of the reactions, R (3) for 15% and R (2) for 0.001%. At $T = 50$ K the fraction of R (3) increases a bit to 22%. Thus, it is clear that the formation of CH_3O is the dominant channel resulting from hydrogenation of H_2CO . Hydrogen

abstraction, R (3), happens with a significant fraction as well, however. The neglect of R (3) by Rimola et al. (2014) may be the reason for the somewhat high fraction of methanol they found compared to observations.

3.5. Kinetic Isotope Effects

Owing to the importance of the deuterium chemistry for tracing dynamic properties of a cloud, we investigated the H/D kinetic isotopic effects (KIEs) for the reactions R (1), R (2) and R (3). The KIE is defined as the ratio of rate constants for the reactions involving the light and the heavy isotopologues, i.e. $\text{KIE} = k_{\text{H}}/k_{\text{D}}$ where k_{H} and k_{D} are the rate constants for the reactions with protium and deuterium. Both the uni-

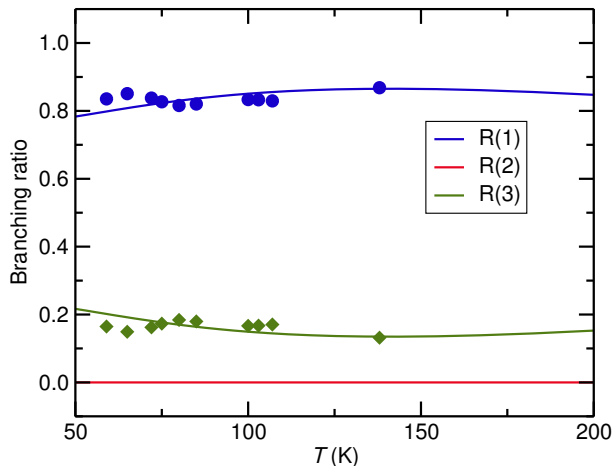


Figure 6. Branching ratios for the three reaction channels of the LH mechanism on an ASW surface. Lines correspond to the fits, symbols to ratios of instanton rate constants.

Table 3. The activation energies (ER mechanism), crossover temperatures and kinetic isotope effects (KIEs) of the deuterium-substituted reactions corresponding to reactions R(1), R(2) and R(3). The energies and temperatures are given K.

| Reactions | V_{act} | E_{act} | T_c | KIEs | | |
|--------------------------|------------------|------------------|-------|------|------|------|
| | | | | 85 K | 75 K | 59 K |
| R(1) D+H ₂ CO | 1420 | 1750 | 141 | 22 | | |
| R(2) D+H ₂ CO | 5220 | 5470 | 280 | 3161 | 4192 | |
| R(3) D+H ₂ CO | 4030 | 2700 | 365 | 7.9 | 9.6 | 12 |
| R(3) H+DHCO | 4030 | 3540 | 288 | 136 | 145 | 165 |
| R(3) D+DHCO | 4030 | 3210 | 273 | 631 | 880 | 1431 |

molecular and the biomolecular surface instanton rate constants are illustrated in Fig. 7. The lines shown in that figure are the fits discussed in detail in Sec. 4.

Compared with the reactions with a protium (H) atom, the ones involving deuterium (D) always have much smaller tunneling rate constants. As frequently observed for tunneling reactions, the KIEs for all three product channels increased with decreasing temperature. The crossover temperature T_c of the reactions with deuterium were reduced to 141 K for the reaction R(1), 280 K for the reaction R(2) and 365 K, 288 K, and 273 K for three cases of the reaction R(3) as shown in Table 3. In that respect, H + DHCO refers to the reaction where D is abstracted by an incoming H atom, D + DHCO means that D is abstracted by an incoming D atom. In addition, this table provides activation energies and

KIEs at chosen temperatures as well. It reveals that the KIEs are strong for all reactions and vary largely from tens to several thousands at low temperatures. Comparing the activation energies including ZPE (E_{act}) in Table 2 and 3, we can find the differences of zero-point energies are not the main reason for strong KIEs which implies tunneling may dominate this phenomenon.

4. IMPLEMENTATION IN ASTROCHEMICAL MODELS

The rate constants calculated in this work can be directly used as input for astrochemical models. To facilitate that, we fitted the calculated tunneling rates with the rate equation (Zheng & Truhlar 2010):

$$k(T) = \alpha \left(\frac{T}{300\text{K}} \right)^\beta \exp \left(-\frac{\gamma(T + T_0)}{T^2 + T_0^2} \right) \quad (2)$$

where α , γ and T_0 are fitting parameters while β is a constant set to one. The pre-exponential factor α has the same unit as the rate constant. Both γ and T_0 have the unit of temperature. The parameter γ is related to the height of the barrier, while T_0 relates to the onset of strong tunneling.

Below the crossover temperature T_c , the instanton rate constants were applied for fitting, while above T_c until 1000 K, rate constants were provided by modified transition state theory where vibrations were treated by quantum harmonic oscillators and tunneling corrections were included by a symmetric Eckart barrier with ω_b and E_{act} taken from the QM/MM calculations. The fitted results were illustrated as lines in Figs. 4 and 7 and the resulting parameters are listed in Table 4. The lines are smooth and match the original data well. We only provide fits to the tunneling rate constants for surface reactions. The fits can be assumed to be reliable from high temperature to approximately the lowest temperature, for which instanton rate constants were available for the specific case, i.e. down to about 60 K for the reactions with H transfer and down to about 40–50 K for reactions involving D-transfer.

For the ER process, the rate constants presented here can directly be used in astrochemical models. In the LH process, there exists the competition between reaction, diffusion out of the site, and desorption from the surface. The probability for reaction is expressed as

$$P_{\text{react}} = \frac{k_{\text{react}}}{k_{\text{react}} + k_{\text{diff}} + k_{\text{desorp}}} \quad (3)$$

where k_{react} is the $k(T)$ we provide in this work, k_{diff} is the sum of the diffusion rate constants of the two species, and k_{desorp} is the sum of the desorption rate constants of the two species. All three of these quantities

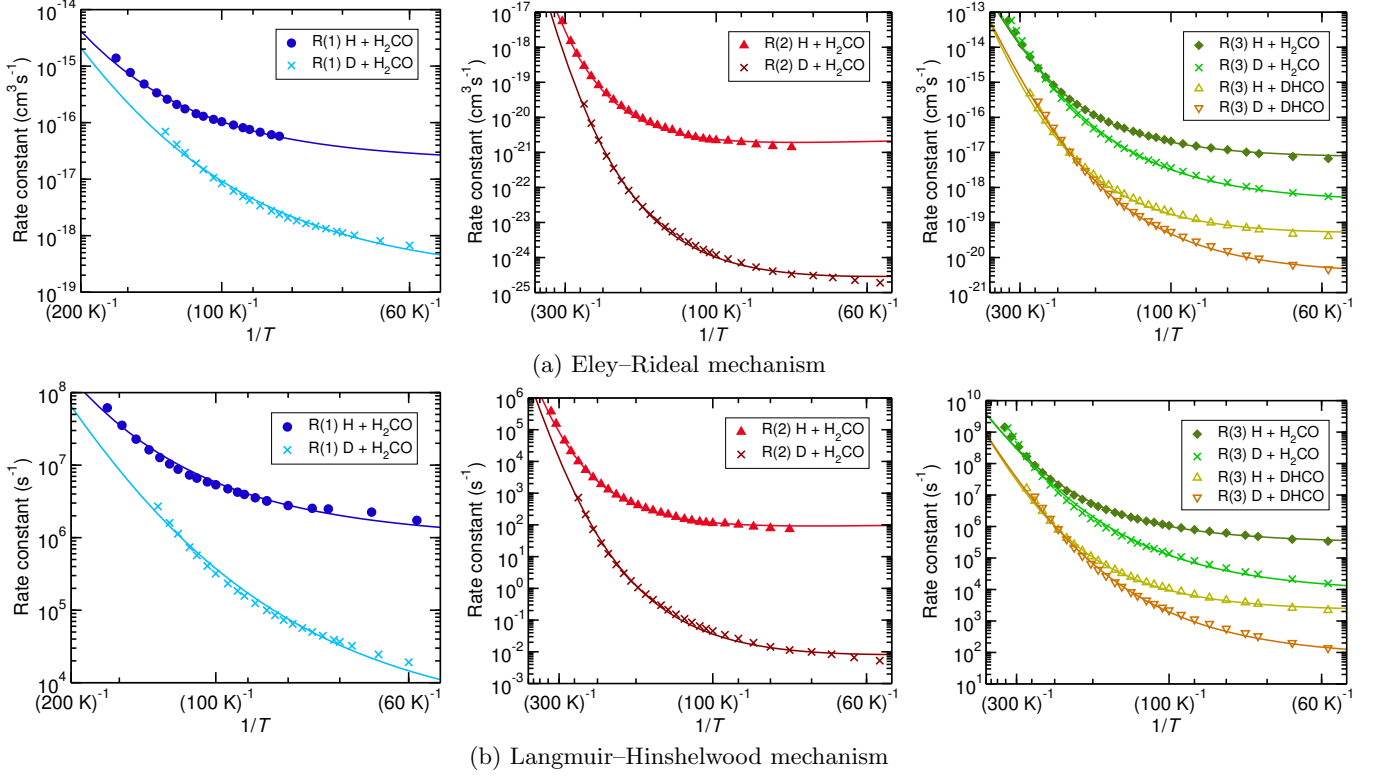


Figure 7. Kinetic isotope effects of the H+H₂CO reactions on the amorphous solid water surface yielding CH₃O, CH₂OH and H₂ + HCO. The markers stand for the calculated instanton rate constants while the lines are the fitted results.

Table 4. Parameters for rate constants described of the reactions R (1), R (2) and R (3) and the corresponding deuterium-substituted reactions by Eq. (2).

| | | H + H ₂ CO | | | D + H ₂ CO | | | H + DHCO | D + DHCO |
|-----------------|---|-----------------------|-------|-------|-----------------------|-------|-------|----------|----------|
| | | R(1) | R(2) | R(3) | R(1) | R(2) | R(3) | R(3) | R(3) |
| ER mechanism | α (10^{-12} cm ³ s ⁻¹) | 3.80 | 2.26 | 6.44 | 2.54 | 1.45 | 6.11 | 5.04 | 3.14 |
| | β | 1 | 1 | 1 | 1 | 1 | 1 | 1 | 1 |
| | γ (K) | 1107 | 3635 | 1597 | 1112 | 3748 | 1538 | 2147 | 1918 |
| | T_0 (K) | 131.1 | 223.8 | 161.0 | 94.5 | 163.4 | 127.1 | 154.9 | 124.1 |
| LH mechanism | α (10^{10} s ⁻¹) | 3.14 | 1.14 | 4.13 | 2.26 | 0.75 | 4.03 | 3.44 | 2.20 |
| | β | 1 | 1 | 1 | 1 | 1 | 1 | 1 | 1 |
| | γ (K) | 830 | 3146 | 1222 | 903 | 3336 | 1226 | 1770 | 1605 |
| | T_0 (K) | 119.6 | 219.3 | 147.7 | 80.0 | 155.3 | 110.9 | 144.6 | 111.2 |

are unimolecular rate constants. The reaction rate of the LH process, used in astrochemical models is

$$R_{\text{LH,react}} = P_{\text{react}} R_{\text{diffusion}}. \quad (4)$$

Here, $R_{\text{diffusion}}$ is the rate by which two species meet on the surface due to diffusion:

$$R_{\text{diffusion}} = \frac{n_{\text{A}} n_{\text{B}}}{n_{\text{sites}}} k_{\text{diff}} \quad (5)$$

where n_{X} is the concentration of species X adsorbed on the surface and n_{sites} is the concentration of adsorption sites. These expressions are valid for n being a volume concentration, a surface concentration, or a number density.

Our data provide k_{react} . If the reaction on the surface in the LH mechanism is faster than diffusion of H atoms to the reactant, the reaction is diffusion-limited.

In that case, $R_{\text{LH,react}} = R_{\text{diffusion}}$ is independent of k_{react} . Then the absolute rate constant will be different from those reported here, but the branching ratio between the three channels should be largely unaffected, R (1) is still expected to dominate the surface process. The binding modes, and consequently blocking of routes for attack, might influence the branching ratio. Here, we only studied one binding site in detail. Since the vast majority was found in binding type (a), which allows access to all three routes, that surface influence can be expected to be small.

5. CONCLUSION

In this paper, we studied three product channels of the reaction $\text{H} + \text{H}_2\text{CO}$, producing CH_3O , CH_2OH , and $\text{H}_2 + \text{HCO}$ on the ASW surface. QM/MM modeling was used combined with instanton tunneling calculations. Three types of binding modes of H_2CO on the ASW surface were found. The binding energies had a broad distribution from ~ 1000 K to 9370 K. The activation barriers were found to be independent of the binding energies. We presented both unimolecular and bimolecular instanton tunneling rate constants for those

three product channels. In all three reactions, we found a significant contribution of quantum tunneling at low temperature. It turned out that the ASW surface has a noticeable catalytic effect, reversing the branching ratio between reactions R (1) and R (3). The ASW surface enhances the formation of CH_3O and hinders hydrogen abstraction to form $\text{H}_2 + \text{HCO}$. The channel leading to CH_2OH is negligible in all cases. In addition, strong kinetic isotope effects were found in all three channels differing between tens to several thousands at low T . Finally, we fitted our calculated rate constants to a modeler-friendly form and provide the fitted parameters for future astrochemical applications.

ACKNOWLEDGMENTS

This work was financially supported by the European Research Council (ERC) under the European Unions Horizon 2020 research and innovation programme (grant agreement No 646717, TUNNELCHEM). The authors also acknowledge support for CPU time by the state of Baden-Württemberg through bwHPC and the German Research Foundation (DFG) through grant no INST 40/467-1 FUGG.

REFERENCES

- Adler, T. B., Knizia, G., & Werner, H.-J. 2007, *J. Chem. Phys.*, 127, 221106
- Althorpe, S. C. 2011, *J. Chem. Phys.*, 134, 114104
- Andersson, S., Goumans, T., & Arnaldsson, A. 2011, *Chem. Phys. Lett.*, 513, 31
- Becke, A. D. 1993, *J. Chem. Phys.*, 98, 1372
- Boogert, A. C. A., Pontoppidan, K. M., Knez, C., et al. 2008, *Astrophys. J.*, 678, 985
- Callan Jr., C. G., & Coleman, S. 1977, *Phys. Rev. D*, 16, 1762
- Chuang, K.-J., Fedoseev, G., Ioppolo, S., van Dishoeck, E., & Linnartz, H. 2016, *Mon. Not. R. Astron. Soc.*, 455, 1702
- Coleman, S. 1977, *Phys. Rev. D*, 15, 2929
- Fedoseev, G., Cuppen, H. M., Ioppolo, S., Lamberts, T., & Linnartz, H. 2015, *Mon. Not. R. Astron. Soc.*, 448, 1288
- Ford, K. E. S., Neufeld, D. A., Schilke, P., & Melnick, G. J. 2004, *Astrophys. J.*, 614, 990
- Gillan, M. J. 1987, *J. Phys. C*, 20, 3621
- Grimme, S., Antony, J., Ehrlich, S., & Krieg, H. 2010, *J. Chem. Phys.*, 132, 154104
- Henkelman, G., & Jónsson, H. 1999, *J. Chem. Phys.*, 111, 7010
- Herbst, E., & van Dishoeck, E. F. 2009, *Annu. Rev. Astron. Astrophys.*, 47, 427
- Humphrey, W., Dalke, A., & Schulten, K. 1996, *J. Molec. Graphics*, 14, 33
- Jorgensen, W. L., Chandrasekhar, J., Madura, J. D., Impey, R. W., & Klein, M. L. 1983, *J. Chem. Phys.*, 79, 926
- Kästner, J., Carr, J. M., Keal, T. W., et al. 2009, *J. Phys. Chem. A*, 113, 11856
- Kästner, J., & Sherwood, P. 2008, *J. Chem. Phys.*, 128, 014106
- Knizia, G., Adler, T. B., & Werner, H.-J. 2009, *J. Chem. Phys.*, 130, 054104
- Langer, J. S. 1967, *Ann. Phys. (N.Y.)*, 41, 108
- Lee, C., Yang, W., & Parr, R. G. 1988, *Phys. Rev. B*, 37, 785
- MacKerell Jr., A. D., Feig, M., & Brooks III, C. 2004, *J. Comput. Chem.*, 25, 1400
- Maret, S., Ceccarelli, C., Caux, E., et al. 2004, *A&A*, 416, 577
- Metz, S., Kästner, J., Sokol, A. A., Keal, T. W., & Sherwood, P. 2014, *WIREs Comput. Mol. Sci.*, 4, 101
- Miller, W. H. 1975, *J. Chem. Phys.*, 62, 1899

- Minissale, M., Moudens, A., Baouche, S., Chaabouni, H., & Dulieu, F. 2016, *Mon. Not. R. Astron. Soc.*, 458, 2953
- Peters, P. S., Duflot, D., Wiesenfeld, L., & Toubin, C. 2013, *J. Chem. Phys.*, 139, 164310
- Peterson, K. A., Adler, T. B., & Werner, H.-J. 2008, *J. Chem. Phys.*, 128, 084102
- Phillips, J. C., Braun, R., Wang, W., et al. 2005, *J. Comput. Chem.*, 26, 1781
- Rappoport, D., & Furche, F. 2010a, *J. Chem. Phys.*, 133, 134105
- . 2010b, *J. Chem. Phys.*, 133, 134105
- Richardson, J. O. 2016, *J. Chem. Phys.*, 144, 114106
- Rimola, A., Taquet, V., Ugliengo, P., Balucani, N., & Ceccarelli, C. 2014, *A&A*, 572, A70
- Rommel, J. B., Goumans, T. P. M., & Kästner, J. 2011, *J. Chem. Theory Comput.*, 7, 690
- Rommel, J. B., & Kästner, J. 2011, *J. Chem. Phys.*, 134, 184107
- Sherwood, P., de Vries, A. H., Guest, M. F., et al. 2003, *J. Mol. Struct. (THEOCHEM)*, 632, 1
- Smith, W., Yong, C., & Rodger, P. 2002, *Mol. Sim.*, 28, 385
- Tielens, A. G. G. M., & Charnley, S. B. 1997, *Origins Life Evol. Biosphere*, 27, 23
- Valiev, M., Bylaska, E. J., Govind, N., et al. 2010, *Comput. Phys. Commun.*, 181, 1477
- Velilla Prieto, L., Sánchez Contreras, C., Cernicharo, J., et al. 2017, *A&A*, 597, A25
- Warshel, A., & Karplus, M. 1972, *J. Am. Chem. Soc.*, 94, 5612
- Warshel, A., & Levitt, M. 1976, *J. Mol. Biol.*, 103, 227
- Weigend, F., & Ahlrichs, R. 2005, *Phys. Chem. Chem. Phys.*, 7, 3297
- Woon, D. E. 2002, *Astrophys. J.*, 569, 541
- Zhao, Y., & Truhlar, D. G. 2005, *J. Phys. Chem. A*, 109, 5656
- Zheng, J., & Truhlar, D. G. 2010, *Phys. Chem. Chem. Phys.*, 10, 7782

Table 1. Benchmark calculations for the reactions R (1), R (2) and R (3).

| Functional | Basis-set | V_{act} (K) | | |
|-----------------------------|-------------|----------------------|-------|-------|
| | | R(1) | R(2) | R(3) |
| (U)CCSD(T)-F12 | cc-pVTZ-F12 | 1570 | 4580 | 3300 |
| PWB6K-D3 | def2-TZVP | 1660 | 4670 | 3200 |
| PWB6K-D3 | def2-SVPD | 1400 | 4280 | 3210 |
| B1B95-D3 | def2-TZVP | 1150 | 3500 | 1510 |
| B1B95-D3 | def2-SVPD | 830 | 3040 | 1500 |
| B3LYP-D3 | def2-TZVP | 40 | 1660 | -330 |
| B3LYP-D3 | def2-SVPD | -300 | 1170 | -290 |
| BECKE97-D-D3 | def2-TZVP | 780 | 1850 | -1670 |
| BECKE97-D-D3 | def2-SVPD | 500 | 1490 | -1510 |
| BHLYP-D3 | def2-TZVP | 820 | 3650 | 2320 |
| BHLYP-D3 | def2-SVPD | 590 | 3310 | 2430 |
| MPWB1K-D3 | def2-TZVP | 1480 | 4400 | 2810 |
| MPWB1K-D3 | def2-SVPD | 1220 | 4000 | 2830 |
| MPW1B95-D3 | def2-TZVP | 1160 | 3560 | 1740 |
| MPW1B95-D3 | def2-SVPD | 840 | 3100 | 1730 |
| PBE0-D3 | def2-TZVP | 550 | 2420 | 1030 |
| PBE0-D3 | def2-SVPD | 310 | 2010 | 1070 |
| PBE96-D3 | def2-TZVP | -270 | 620 | -1190 |
| PBE96-D3 | def2-SVPD | -670 | 30 | -1310 |
| PW6B95-D3 | def2-TZVP | 960 | 3310 | 1390 |
| PW6B95-D3 | def2-SVPD | 620 | 2830 | 1360 |
| SSB-D-D3 | def2-TZVP | 40 | 1480 | -570 |
| SSB-D-D3 | def2-SVPD | -380 | 1020 | -680 |
| TPSS-D3 | def2-TZVP | -2070 | -600 | -2530 |
| TPSS-D3 | def2-SVPD | -2280 | -1020 | -2490 |
| TPSSH-D3 | def2-TZVP | -1760 | 80 | -1730 |
| TPSSH-D3 | def2-SVPD | -1930 | -310 | -1670 |
| (U)CCSD(T)-F12 ^a | cc-pVTZ-F12 | 1770 | 4910 | 3540 |
| PWB6K-D3 ^a | def2-TZVP | 1620 | 4780 | 3320 |

^aStructures from the geometry optimization based on PWB6K-D3/def2-TZVP theory level

APPENDIX

A. DATA FOR THE BENCHMARK CALCULATIONS

Results of the benchmark calculations are given in Table 1. The functional/basis set combination PWB6K-D3/def2-TZVP resulted in activation energies closest to the (U)CCSD(T)-F12/cc-pVTZ-F12 reference data and was, therefore, chosen for the present study.